Supporting Information

Multifunctional Chitosan Tailored γ-Aluminum Oxy-hydroxide monolith Aerogels for Sustained Environmental Remediation

*Prashant D. Sarvalkar[a], Anuj S. Jagtap[a], Apurva S. Vadanagekar[a], Suhas S. Kamble[a], Arati P. Tibe[a], Arif D. Shiekh[a], Rajiv S. Vhatkar[b], Kiran Kumar K. Sharma[a]**

[a]School of Nanoscience and Biotechnology, Shivaji University, Kolhapur-416004 (MH), India.

[b]Department of Physics, Shivaji University, Kolhapur-416004 (MH), India.

*Corresponding author

Email: kks.snst@unishivaji.ac.in

1. Methodology

1.1 Synthesis of an aluminium alkoxide-based γ-AlOOH aerogel

Aluminum tri-sec-butoxide (6.37 mL), ethanol (23.38 mL), and water (0.25 mL) were used to prepare 30 mL of Solution A, and the mixture was constantly stirred for 90 min at 60 °C to complete the hydrolysis of ASB. Initially, the solution appeared cloudy; however, upon completion, it became clear. The optimized molar ratio for the ASB sol was 1:16:0.6 for aluminum tri-sec-butoxide, ethanol, and water. Solution B was prepared by mixing 6.07 mL of methanol with 0.072 mL of water in a beaker and stirring for 15 min. Solution B was then added to solution A and the mixture was stirred for 30 min. that, 1.20 mL of acetic acid was added to the above mixture. The sol was then transferred into a mold and agitated for 3 h to form a gel.

The influencing parameters in the sol-gel (hydrolysis and condensation) method are the ratio of aluminum tri-sec-butoxide to ethanol and water, as well as the volume and concentration of the catalyst and solvent. During hydrolysis, the H_2O molecules split into H^+ and OH^- ions. A schematic representation of the ASB aerogel synthesis is shown in Scheme S1a. The ASB sol was formed in two stages: (i) hydrolysis and (ii) condensation. After hydrolysis, the OH^- group replaces the secondary butoxide ($–OC_4H_9$) group from aluminum tri-second butoxide ($OC_4H_9–Al=(OC_4H_9)_2$),

bonding with Al^{3+} to form aluminum tri-hydroxide (OH–Al = $(OH)_2$). The remaining sec-butoxide group reacts with the H^+ ion to produce 2-butanol (C_4H_9OH) as a byproduct. The n =Al-OH groups bond together during the condensation stage, resulting in the formation of an "Al-O-Al" bridge and H_2O.

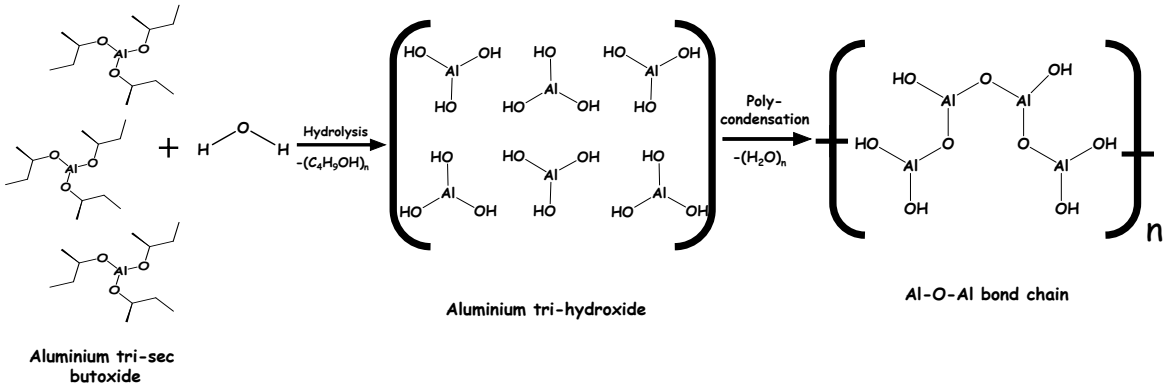

Scheme S1a: The schematic representation of ASB aerogel synthesis via sol-gel method.

2.2.2 Synthesis of an aluminium salt-based γ-AlOOH aerogel

Firstly, 5.92 g of ($AlCl_3.6H_2O$) or 4.6 g of ($Al(NO_3)_3.9H_2O$) was dissolved in 2 mL H_2O and 18 mL of ethanol solution, and the mixture was constantly stirred for 30 min. Subsequently, 1 mL of DMF was added to the above solution. DMF acts as a drying control additive (DCA). In the solution, add 6.7 mL of PO, which acted as a gelation agent, was added to the solution. The gelation time varied with the PO variation. With an optimized PO and aluminium precursor molar ratio of 1:8, a gel was formed within 2 h. Propylene oxide was added as an acid scavenger to promote the gel formation [40].

A schematic representation of the aluminum salt, that is, aluminum nitrate or aluminum chloride-based γ-AlOOH aerogel (AN and AC aerogel, respectively) synthesis, is shown in Scheme S1b. A solvent is utilized to dissolve aluminum salts, leading to the dissociation of the aluminum salt into aluminum cations (Al^{3+}) and corresponding anions (Cl_3^- or NO_3^-). The organic component, specifically the epoxide compound, reacts with aluminum species, resulting in the formation of a gel. When hydroxide ions (OH^-) are present due to the dissociation of water, they initiate an attack on the epoxide ring, resulting in its subsequent opening. The covalent bonding between the oxygen atom (from the epoxide ring) and the aluminum cation leads to the integration of aluminum species into the organic compound. The interaction between aluminum cations and

epoxide compounds results in the formation of a three-dimensional network structure. The formation of crosslinks between the aluminum species and organic compound is responsible for the gelation of the system[41,42].

A. Hydrolysis:

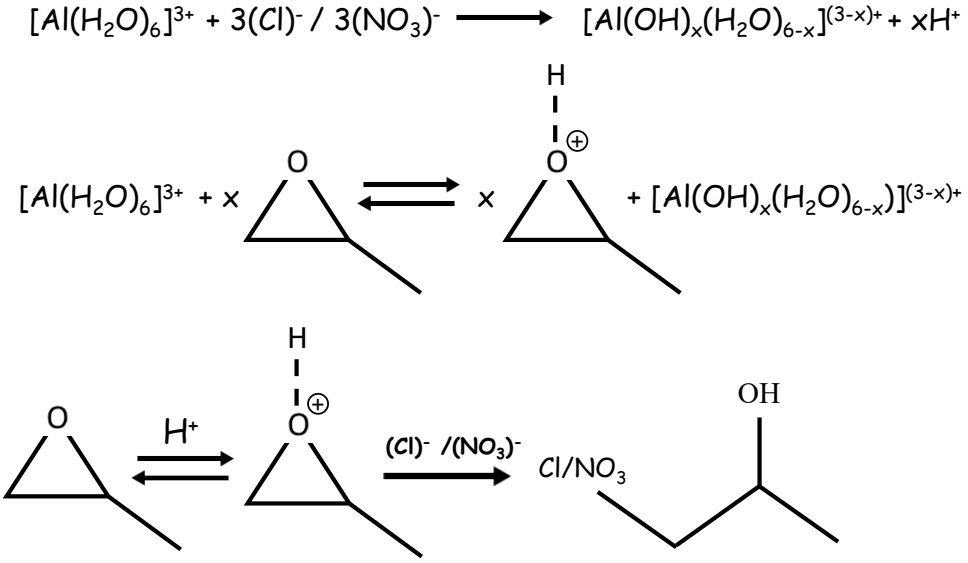

B. Condensation

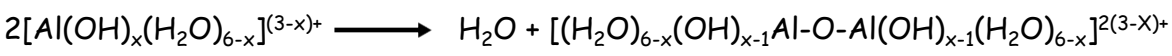

Scheme S1b: The schematic representation of the aluminum salt-based alumina aerogel synthesis mechanism.

2. XRD. The XRD pattern of the as-synthesized γ-AlOOH aerogel with different precursors of aluminum and chitosan content (Figure S1a-c) shows the same XRD characteristic peak of γ-AlOOH (pseudo-boehmite). Figure S1d shows the orthorhombic crystal structure of γ-AlOOH visualized using VESTA software.

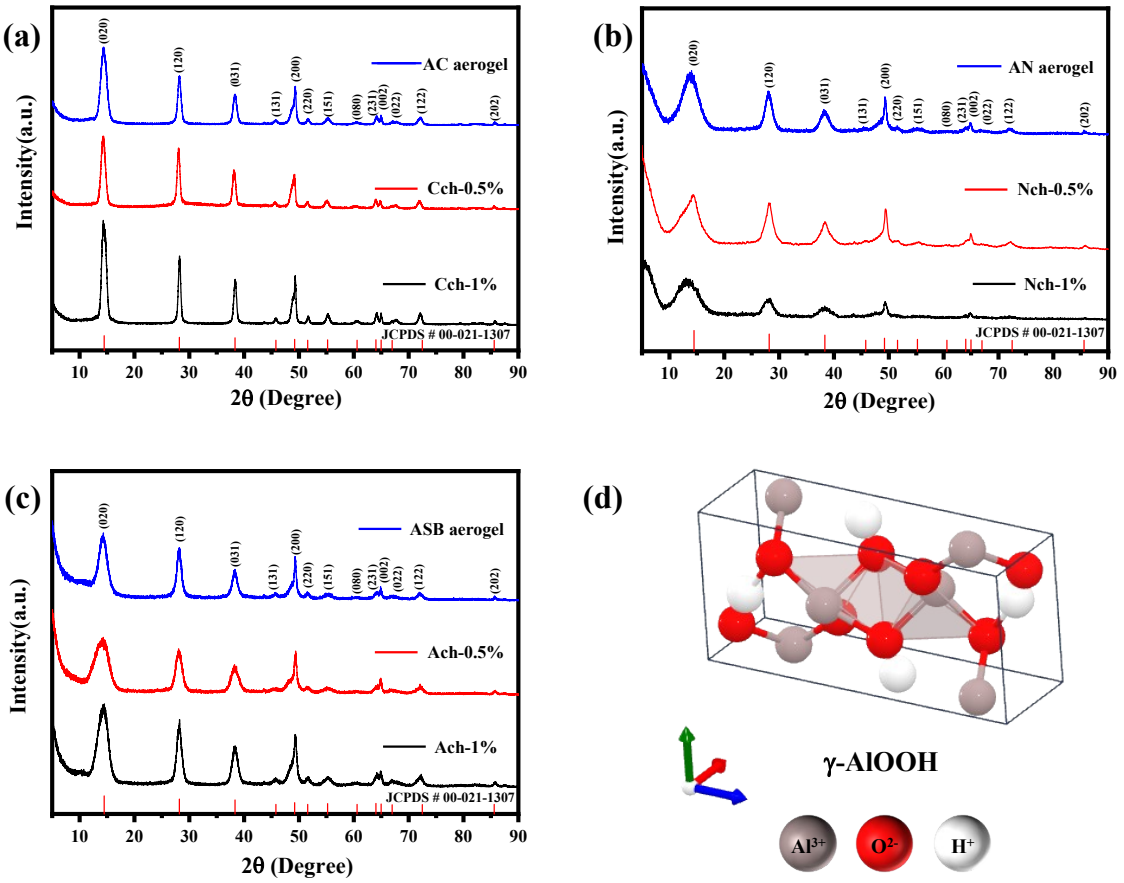

Figure S1: XRD spectra of ASB aerogel with different precursors of aluminium and chitosan content variation (a) XRD spectra of optimized chitosan tailored γ-AlOOH aerogel using aluminium chloride hexahydrate precursor (b) XRD spectra of optimized chitosan tailored γ-AlOOH aerogel using aluminium nitrate nonahydrate precursor (c) XRD spectra of optimized chitosan tailored γ-AlOOH aerogel using aluminium tri sec butoxide (ASB) precursor. (d) Orthorhombic crystal structure of γ-AlOOH is visualised by VESTA software.

3. FTIR. The FTIR spectra of chitosan, depicted in Figure S2, display several characteristic peaks corresponding to different functional groups and molecular vibrations. The broad peak

observed at 3450 cm^{-1} is attributed to the O-H stretching vibration and the Amide A band, which corresponds to N-H stretching. The absorption bands within the range of 2849–2916 cm^{-1} are indicative of asymmetric C-H stretching. At 1652 cm^{-1}, A prominent band was identified at 1652 cm^{-1}, which corresponded to the amide I band, primarily associated with the C=O stretching of secondary amides. The absorption peak at 1557 cm^{-1} is characteristic of the amide II band, arising from C-N stretching and N-H bending vibrations. Additionally, the band at 1376 cm^{-1} is attributed to the amide III band, involving both C-O and C-N stretching vibrations. Finally, the peaks at approximately 1060 cm^{-1} are indicative of asymmetric C-O stretching vibrations[58,59].

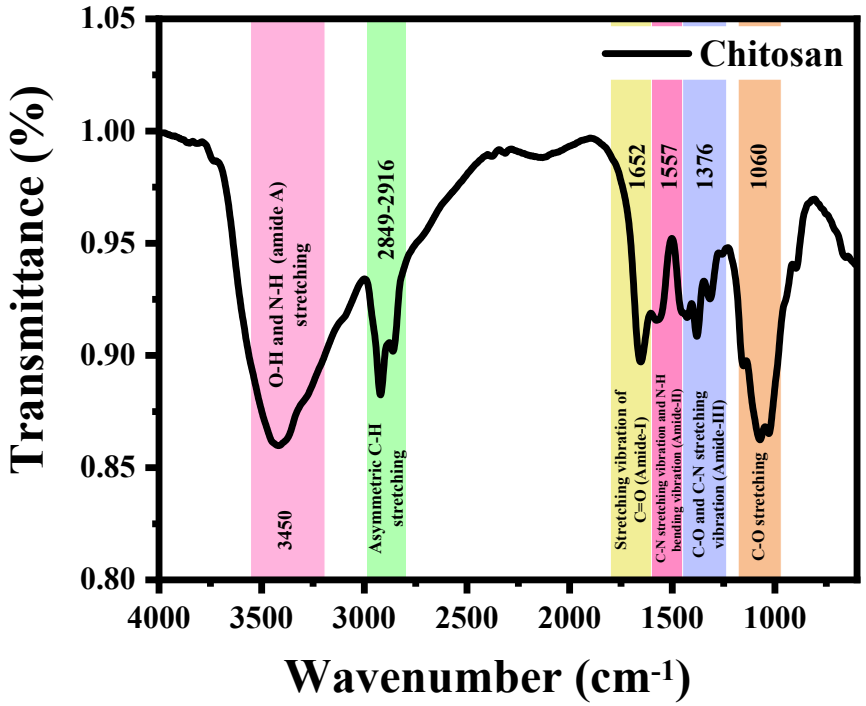

Figure S2: FTIR spectra of chitosan.

The growth of peaks at 1387 and 1456 cm^{-1} in Figures S3a–c indicates a change in the concentration of chitosan in the γ-AlOOH aerogel[58]. The band at 1065–1080 cm^{-1} correspond to Al-O-H. The boehmite structures 4 (AlO_4) and 6 (AlO_6)-coordinated Al-O bonds correspond to the peaks from 482 to 890 cm^{-1}, which are also known as the characteristic peaks of the boehmite structure [60]. The band at 875 cm^{-1} is ascribed to (AlO)O-H angle bending. The band at 725-785 cm^{-1} was due to the Al-O stretching mode. The O-Al-O bending mode was observed at 630 cm^{-1}, while the Al-O boehmite mode was observed at 485 cm^{-1}[61,62].

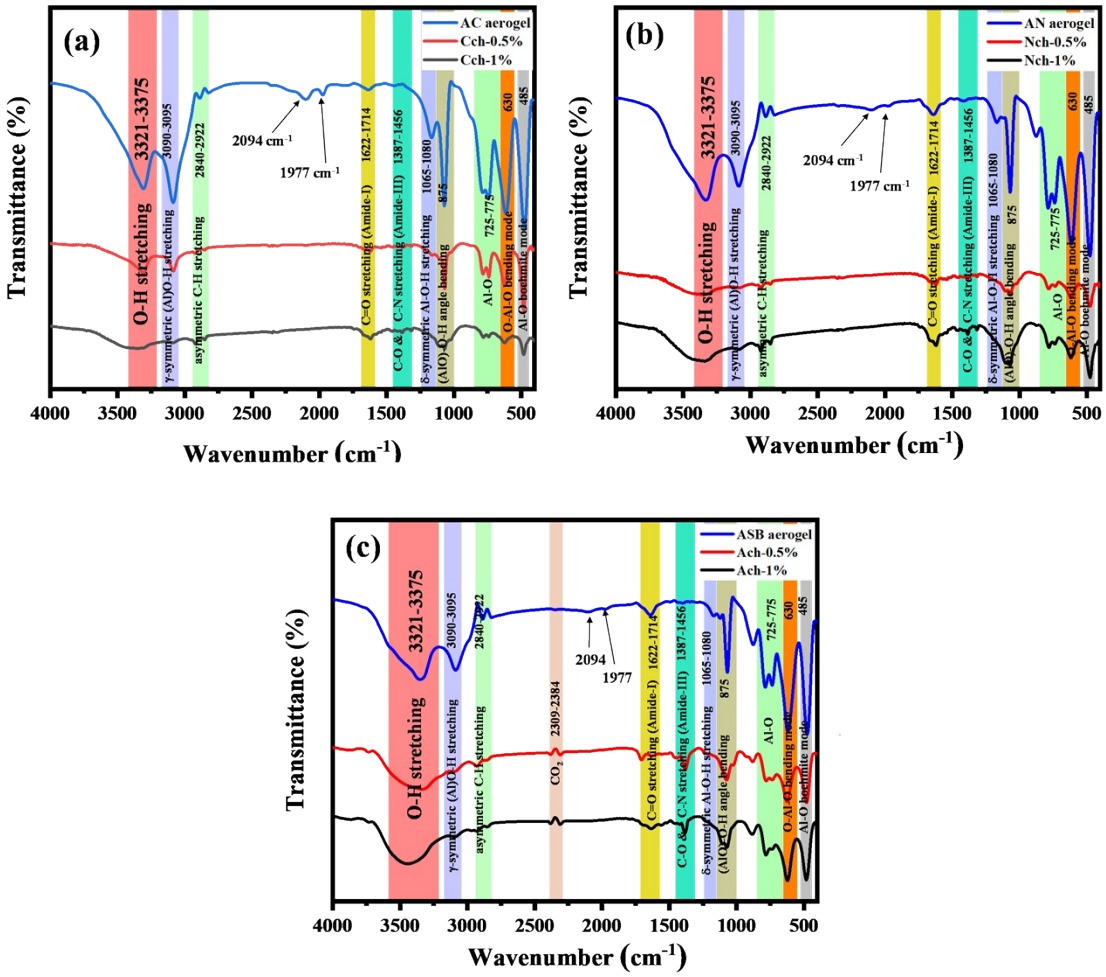

Figure S3: FTIR spectra of γ-AlOOH aerogel with different precursors of aluminium and chitosan content variation (a) FTIR spectra of optimized chitosan tailored γ-AlOOH using aluminium chloride hexahydrate precursor (b) FTIR spectra of optimized chitosan tailored γ-AlOOH aerogel using aluminium nitrate nonahydrate precursor (c) FTIR spectra of optimized chitosan tailored γ-AlOOH aerogel using aluminium tri sec butoxide (ASB) precursor.

4. TG-DTA Curve. Figure S5 represents the TGA-DTA thermogram of pristine chitosan, which reveals two distinct stages of decomposition. The first stage, from 25°C and 120°C, corresponds to a weight loss of 9.3% possibility due to the loss of water associated water molecules, while the second stage, between 270°C and 350°C, corresponds to a weight loss of 51.75%, which could be attributed to the breakdown of chitosan including decomposition of the

saccharide structure, and polymerization of deacetylated units[48]. The TGA-DTA analysis reveals that chitosan is stable with no significant weight loss up to 280°C. The study aimed to assess the temperature stability of pristine chitosan, relevant to our supercritical drying process at 243°C. Results show chitosan remains stable up to 270°C, confirming its suitability for the process without significant degradation. Figure S6a-b shows the TG-DTA thermograms of synthesized ASB and Ach-1% aerogels, each consisting of two stages. The first stage, between 25°C and 200°C, corresponds to a weight loss of 6.5% to 7.3% due to the evaporation of residual ethanol and water molecules. In the second stage, ASB aerogel (Figure S6a) shows a significant weight loss of approximately 26.51% between 350°C and 600°C, with an exothermic peak at 490.2°C attributed to the phase transition from AlOOH to Al_2O_3[47]. Ach-1% aerogel (Figure S6b) demonstrates a weight loss from 300°C to 1000°C, with sub-stages involving the degradation of the polysaccharide structure of chitosan and an exothermic peak at 495.23°C, and the evaporation of water during the conversion of γ-AlOOH to Al_2O_3 and pyrolyzed carbon from chitosan residual.

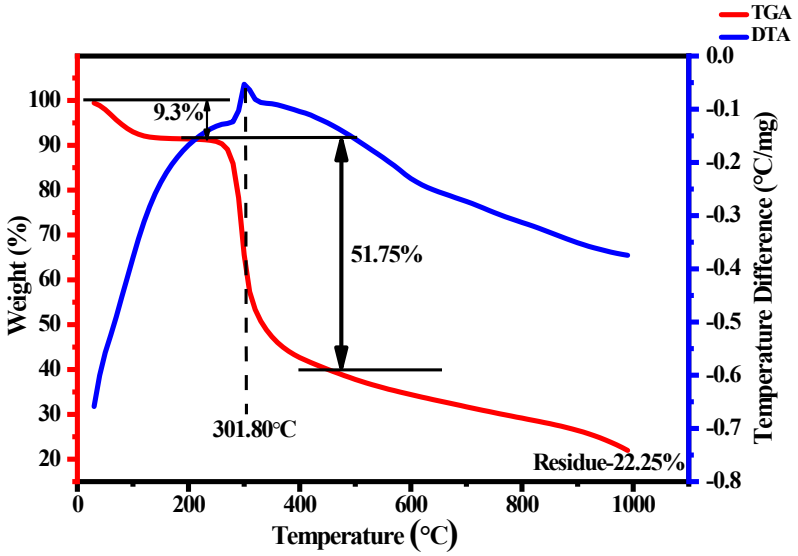

Figure S4: TGA-DTA thermogram of chitosan.

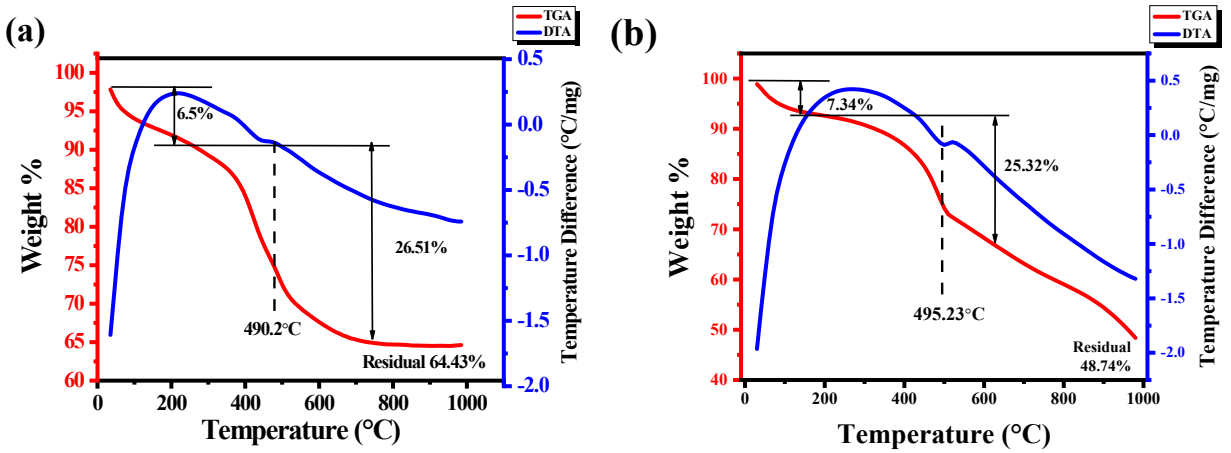

Figure S5: TGA-DTA thermograms of (a) ASB aerogel and(c) Ach-1% aerogel.

5. Morphology Study. A description of the EDS spectra and quantitative analysis of the ASB and Ach-1% aerogels is shown in Figures S6a and S6b. According to the EDAX spectrum in Figures S6a, Al and O were identified in the sample of the ASB aerogel. Furthermore, it is clear that the Ach-1% aerogel (Figures S6b) was synthesized without impurities, confirming the presence of Al, C, O, and N. The absorption peak of aluminium was 1.5 keV. Figures S6a shows that the Al% in the ASB aerogel was 50.02 and the O% was 49.98. Figures S6b shows that the Ach-1% aerogel was composed of 39.73% Al, 23.35% C, 36.03% O, and 0.89% N.

The elemental mapping of the Ach-1% (Figure S7a-e) aerogel reveals the presence of C (Figure S7b), Al (Figure S7c), O (Figure S7d), and N (Figure S8e). The elemental mapping of the ASB aerogels is depicted in Figure S8a-c, indicating elements such as Al (Figure S8b) and O (Figure S8c). The presence of C and N confirmed the presence of dispersed chitosan in the ASB aerogel. From elemental mapping, we concluded that chitosan was equally dispersed throughout the ASB aerogel, resulting in chitosan tailored to the aerogel structure with no additional impurities. A conductive carbon-coated copper grid was used to prepare the aerogel sample for TEM analysis. Although the substrate contains a layer of C, EDAX cannot determine the presence of C in the sample and provide a uniform layer throughout the map. The TEM images revealed a uniform distribution of chitosan within the aerogel, while the EDAX spectra indicated the presence of characteristic elements associated with chitosan. Elemental mapping further supported these findings by showing a homogeneous dispersion of chitosan throughout the γ-AlOOH aerogel structure.

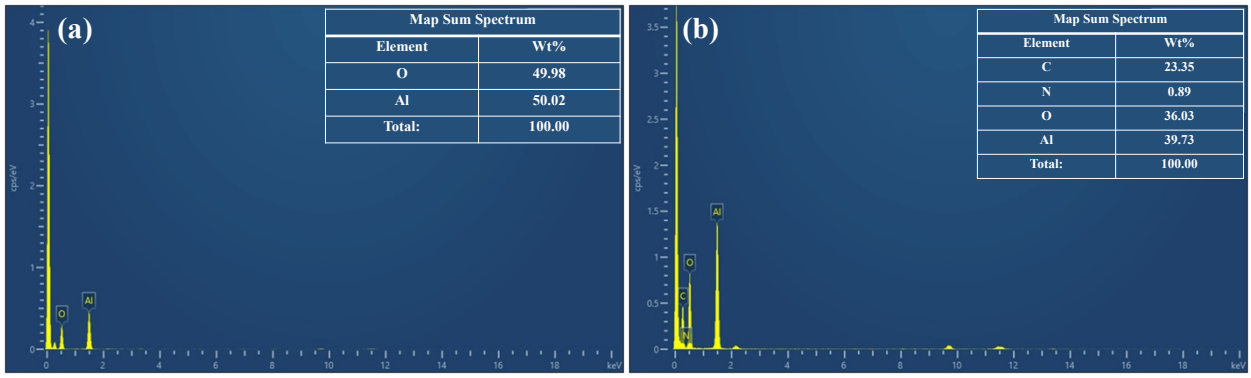

Figure S6: EDAX spectra of (a) ASB and (b) Ach-1% aerogel.

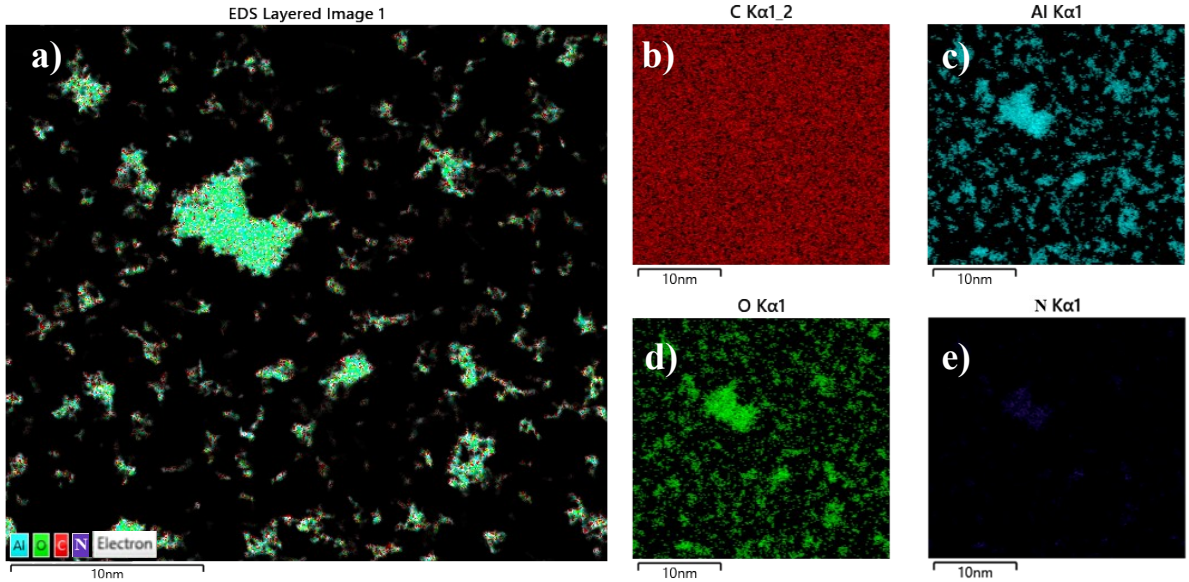

Figure S7: TEM/EDS Elemental mapping of (a-e) Ach-1% aerogel. Elemental Mapping of (b) C Map, (c) Al Map, (d) O Map, (e) N Map.

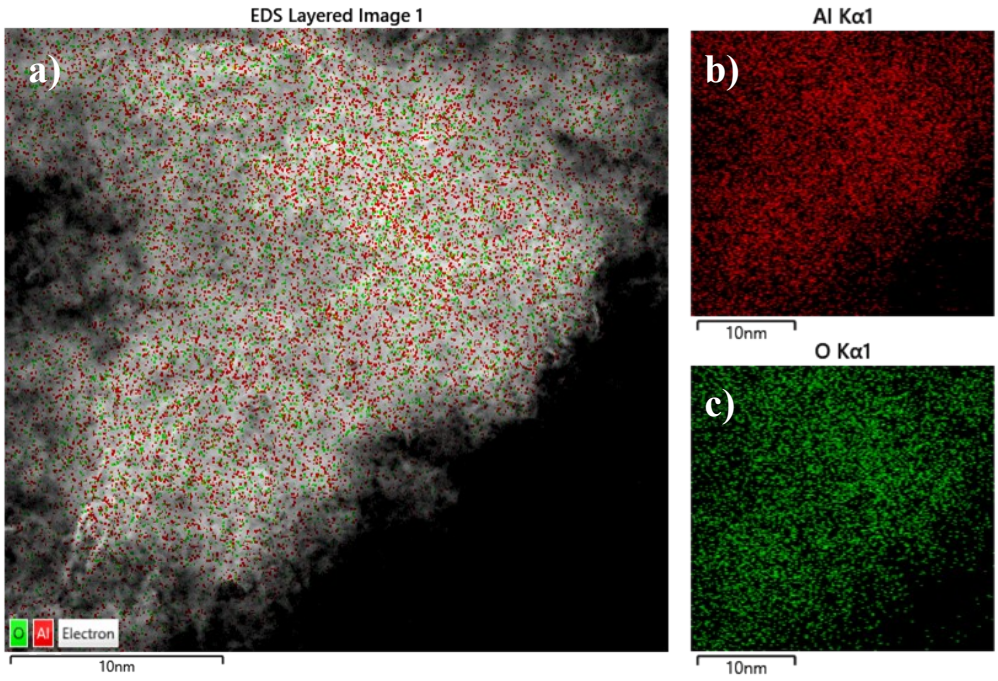

Figure S8: TEM/EDS Collective Elemental mapping of (a-c) ASB aerogel (ASB precursor used). Individual Elemental Mapping of (b) Al Map and (c) O Map.

6. Effect of pH. Table S1 displays the results of the point of zero charge (pzc) investigations conducted on the synthesized aerogels, covering a pH range of 2 to 11.

Table S1: pzc value of all synthesized aerogels

Sr. No.	Name of the materials	pzc value for pH solution
1.	**AC aerogel**	7.73
2.	**Cch-0.5% aerogel**	3.78
3.	**Cch-1% aerogel**	4.64
4.	**AN aerogel**	8.30
5.	**Nch-0.5% aerogel**	4.81

6.	**Nch-1% aerogel**	4.44
7.	**ASB aerogel**	4.15
8.	**Ach-0.5% aerogel**	3.83
9.	**Ach-1% aerogel**	3.80

Figure S9 illustrates the changes in the color of MB and CV across initial pH levels ranging from 2 to 11. Variations in the absorbance of dyes and heavy metal ions indicate changes in pH levels[1]. MB, an azo dye with a pKa of 3.8, and CV, with pKa values of 5.31 and 8.64, are predominantly present within this pH range[2].

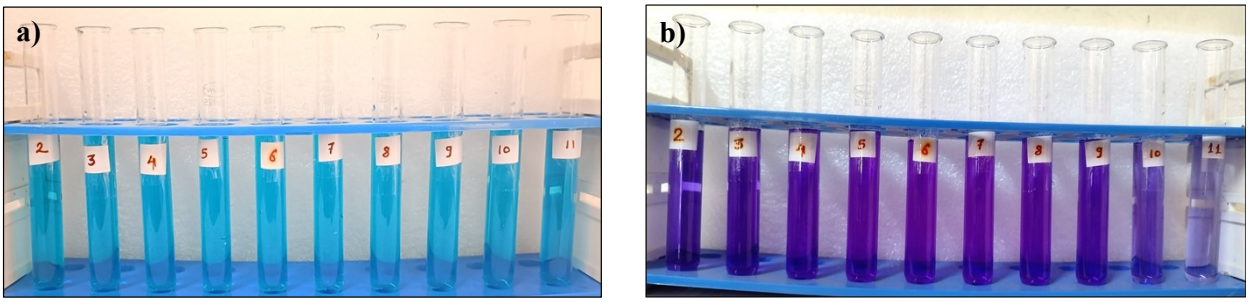

Figure S9: Initial images of dye solutions adjusted from 2 to 11 pH: (a) MB and (b) CV dye solutions.

We observe the pzc for ASB and Ach-1% aerogels at 4.15 and 3.80, respectively. The more acidic pzc value of the Ach-1% aerogel, compared to the ASB aerogel, is due to the residual acetic acid used in its preparation. At a pH of 7, MB dye demonstrates the highest dye removal efficiency among all synthesized aerogels. Given that the dye removal efficiency drops below 80% at pH levels above 8, we identify pH 7 as the optimal condition for MB adsorption (see Figure 5a). We also estimate that the highest effective pH for CV adsorption is 7, beyond which the ratio of CV decrease becomes variable. Between pH levels of 7 and 8, the surface of the adsorbents is positively charged (refer to Figure 5b).

At a pH of 5, the nitrogen and oxygen atoms within the adsorbent's functional groups, which possess lone pairs of electrons capable of forming coordination interactions with Pb(II) ions, significantly enhanced the efficiency of Pb(II) ion removal by Ach-1% (Figure 5c). Additionally, the acidic conditions lead to the protonation of amine and hydroxyl groups on the adsorbent surface, inducing electrostatic repulsion that negatively impacts the adsorption of Pb(II) ions.

Furthermore, competition between H^+ ions and Pb(II) ions for adsorption sites exacerbates this effect. The formation of $Pb(OH)^+$ and $Pb(OH)_2$ species contributes to the observed decrease in adsorption efficiency beyond a pH of 6.

The pH significantly influences the solubility and speciation of U(VI) in solution, as well as the overall charge of the adsorbent. In strongly acidic conditions, the competition between protons and U(VI) ions decreases, impairing the adsorption of uranyl ions by the adsorbent and diminishing the material's removal performance. However, as the pH increases to 6, where the removal efficiency peaks at 99.55%, the adsorption capability improves markedly. Beyond pH 7, the efficiency of U(VI) removal begins to decline, primarily due to the precipitation of $UO_2(OH)_2$, complicating the formation of stable complexes with the OH and NH_2 functional groups on the Ach-1% adsorbent's surface[3]. Consequently, pH 7 has been identified as the optimal condition for U(VI) removal[4]. The adsorption process, influenced by the pH, affects both the speciation of U(VI) in the solution and the protonation/deprotonation dynamics of the NH_2 and OH groups on the adsorbents. At pH 7, Figure 5d illustrates a notable enhancement in U(VI) removal efficiency using synthesized aerogels, achieving maximum efficiencies of over 95.8%. Below a pH of 3.0, UO_2^{2+} species predominate, comprising approximately 94% of the total U(VI) [5,6]. Between pH 4 and 8, the solution exhibits a variety of hydroxyl complexes of U(VI), including $UO_2(OH)^+$, $UO_2(OH)^+_{(aq.)}$, $(UO_2)_2(OH)_2^{2+}$, $(UO_2)_3(OH)_5+$, and $(UO_2)_4(OH)_7^+$. Notably, at pH 7.0 and 6.0, $(UO_2)_3(OH)_5^+$ becomes the predominant form, accounting for approximately 68.14% and 74.50% of U(VI) species, respectively. Above pH 8.0, $(UO_2)_3(OH)_7^-$ becomes prevalent, highlighting the complex nature of U(VI) speciation and its dependence on pH[4].

Arsenite (As(III)) is a highly mobile substance that increases its mobility in acidic environments, particularly when the pH is below 7 (Figure 5e). Its uncharged state, H_3AsO_3, reduces adsorption to mineral surfaces, enhancing its solubility and mobility in aquatic systems. This is due to a lack of charge, which induces electrostatic repulsion between neutral arsenite species and negatively charged adsorbent surfaces. The presence of hydrolyzed arsenate species, such as $H_2AsO_4^-$ and $HAsO_4^-$, intensifies this competition, influencing adsorption dynamics[7,8]. As pH increases, arsenite undergoes deprotonation, forming more negatively charged species and increasing its adsorption affinity towards positively charged surfaces. However, under highly alkaline conditions, the dominance of competing anions and the negative charge on adsorbent surfaces alter arsenic speciation and mobility, potentially reducing adsorption efficacy. The study

identifies pH 7 as the optimal condition for maximizing As(III) removal, suggesting a critical equilibrium between arsenite solubility and adsorption site availability. This equilibrium is crucial for developing effective arsenic remediation strategies in water treatment processes[8].

Table S2 provides the zeta potential values for all adsorbents and adsorbates.

Table S2: The zeta potential values for all adsorbents and adsorbates.

Sr. No.	Name of the materials	pH of solution	Before adsorption (aqueous solutions) Zeta potential value (mV)	After adsorption (aqueous solutions) Zeta potential (mV)
1.	**AC aerogel (1 mg/ml)**	-	+32.18	+0.7 (for MB)
2.	**Cch-0.5% aerogel (1 mg/ml)**	-	+31.35	+1.1 (for MB)
3.	**Cch-1% aerogel (1 mg/ml)**	-	+29.66	+1.5 (for MB)
4.	**AN aerogel (1 mg/ml)**	-	+30.20	+0.8 (for MB)
5.	**Nch-0.5% aerogel (1 mg/ml)**	-	+29.71	+0.7 (for MB)
6.	**Nch-1% aerogel (1 mg/ml)**	-	+26.23	+1.4 (for MB)
7.	**ASB aerogel (1 mg/ml)**	-	+42.2	+1.8 (for MB)
8.	**Ach-0.5% aerogel (1 mg/ml)**	-	+29.25	+2.1 (for MB)
9.	**Ach-1% aerogel (1 mg/ml)**	-	+28.67	-
10.	**MB (1 ppm) + Ach-1% aerogel (1 mg/ml)**	7.0	-9.61	+1.0
11.	**CV (1 ppm) + Ach-1% aerogel (1 mg/ml)**	7.0	-8.0	+1.2
12.	**Pb(II) (1 ppm) + Ach-1% aerogel (1 mg/ml)**	5.0	-1.2	+0.8
13.	**U(VI) (1 ppm) + Ach-1% aerogel (1 mg/ml)**	7.0	-19.3	+0.6
14.	**As(III) (1 ppm) + Ach-1% aerogel (1 mg/ml)**	7.0	-14.4	+1.2

7. Initial dye concentration impact. Figure 6a-e shows that the adsorption capacity of Ach-1% aerogel, a specifically engineered adsorbent, increased significantly at higher pH levels. Specifically, at a pH of 7, the equilibrium adsorption capacity (*Qe*, mg/g) for MB dye was 37.87 mg/g using the ASB aerogel and 118.66 mg/g with the Ach-1% aerogel. CV dye showed similar trends, with *Qe* values of 36.83 mg/g for ASB and 119.06 mg/g for Ach-1% aerogel, suggesting enhanced adsorption in neutral (pH 7) conditions. Further analyses extended to the adsorption of heavy metal ions, revealing the superior performance of Ach-1% aerogel in removing Pb(II) at pH 5, with a Qe of 36.38 mg/g, and As(III) and U(VI) at pH 7, with Qe values of 68.79 mg/g and 475.14 mg/g, respectively. These results were marginally (i.e., 1.15 to 1.7 folds) higher than those achieved with the pristine γ-AlOOH aerogel, illustrating the exceptional potential of the Ach-1% aerogel as an efficient medium for water decontamination from both dyes and heavy metal ions, as shown in Figure S10a-j.

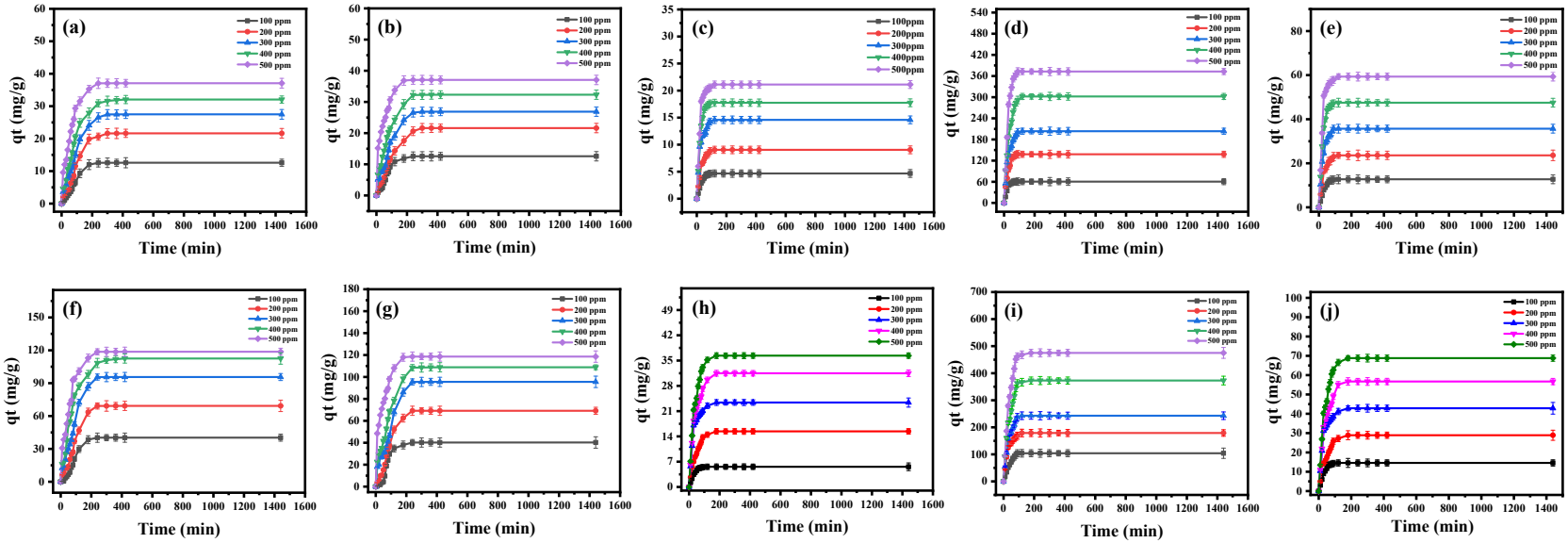

Figure S10: Plot of adsorption at time 't' (qt) against incubation time for (a) MB on ASB, (b) CV on ASB, (c) Pb(II) on ASB, (d) U(VI) on ASB, (e) As(III) on ASB, (f) MB on Ach-1%, (g) CV on Ach-1%, (h) Pb(II) on Ach-1%, (i) U(VI) on Ach-1%, and (j) As(III) on Ach-1%.

8. Adsorption Isotherms.

Langmuir isotherm

As a result, the adsorption and desorption kinetics were comparable at equilibrium. Equation (2) represents the Langmuir isotherm model for the nonlinear form:

$$q_{e=} \frac{q_{max}\ K_L C_e}{1 + K_L C_e} \quad \ldots\ldots (2)$$

where *qe* (mg/g) is the amount of adsorbate per unit mass of adsorbent at equilibrium, q_{max} (mg/g) is the maximum adsorption capacity of the absorbents, and constant the Langmuir adsorption is K_L (L/g). To determine if the isotherm and dye adsorption are favorable, the equilibrium parameter R_L is taken into consideration, as given in Equation (3).

$$R_{L\ =} \frac{1}{1 + K_L C_o} \quad \ldots\ldots (3)$$

where the initial concentration of the dye is C_o (mg/L), and the constant of Langmuir isotherm adsorption is K_L (L/g). If R_L values lie between 0 and 1, then the adsorption is considered successful, and the adsorption process is not favorable if the value is greater than 1.

Freundlich adsorption isotherm

In the field of adsorption, the Freundlich adsorption isotherm is an empirical model that characterizes nonideal and reversible adsorption onto heterogeneous surfaces. Unlike models that assume a single layer of adsorbate, the Freundlich isotherm describes adsorption where multiple layers can form and does so without limiting the process to monolayer adsorption. Introduced in 1909, this model highlights the heterogeneous nature of adsorptive surfaces by accounting for the variable affinities and nonuniform distribution

of heat generated upon adsorption[82]. The affinities distributed across these heterogeneous surfaces illustrate the complexity of the adsorption dynamics captured by the Freundlich isotherm. The Freundlich isotherm equation for the non-linear form is given (Equation (4)) as follows:

$$q_{e=} K_F C_e^{1/n} \quad \text{…....(4)}$$

where *qe* (mg/g) is the amount of adsorbate per unit mass of adsorbent at equilibrium, and K_F is the approximate capacity of adsorption. Adsorption is considered chemical when $1/n < 1$, while the value of $1 < 1/n < 10$ physical adsorptions is far more supported. The non-linear relationship between the 'q_e' (mg/g) and the 'C_e' is depicted in Figure 7a–e. The Freundlich isotherm, which is particularly relevant for adsorption processes involving organic chemicals or compounds with significant variability on heterogeneous adsorbents, provides a model for these interactions. Notably, the exponent of the isotherm ($1/n$) serves as an indicator of the adsorption mechanism: values of $1/n$ less than 1 suggest chemisorption, whereas values greater than 1 suggest physisorption, highlighting the utility of the model in distinguishing between these two adsorption types. This versatility makes the Freundlich isotherm a widely adopted model for analyzing adsorption phenomena, as illustrated in the plots of 'q_e' against 'C_e' in Figure 7a–e.

Temkin Adsorption Isotherm

The Temkin Adsorption Isotherm posits a linear decrease in the heat of adsorption across the adsorbent surface, rather than the constant heat of adsorption assumed by other isotherms. This model suggests that the adsorbate-adsorbent interactions lead to a decrease in adsorption energy, thus affecting the distribution of molecules on the adsorbent surface. Unlike models requiring a rigidly structured adsorption phase, the Temkin isotherm acknowledges the heterogeneity of real surfaces, making it suitable for analyzing adsorption where the adsorption energy uniformly decreases. However, its simplicity and the assumptions underpinning it limit its application in modeling more complex adsorption phenomena, where the variation in adsorption energy is not linear or uniform across the adsorbent surface[14]. By plotting the sum of adsorbed q_e against C_e and determining Q_m and K_T, as required by the formulation (Figure 7a–e), these parameters were determined. The Timken's equation model is given by Equation (5).

$$q_{e=} Q_m ln(K_T C_e) \quad \text{……..(5)}$$

Where $Q_m = RT/b_T$ (J/mol) and the universal gas constant (8.314 J/mol. K) is denoted as R, the temperature is denoted as T (298 K), the adsorption heat parameter b_T (J/mol), the binding constant of the Temkin equilibrium (L/g) is denoted as K_T and constant, the amount of adsorbate adsorbed is denoted as q_e (mg/g), and the adsorbate equilibrium concentration is denoted as C_e (mg/mL).

S11a-j compare the performance of the Langmuir, Freundlich, and Temkin adsorption isotherm models with various adsorbates such as MB, CV, Pb(II), U(VI), and As(III) on both ASB and Ach-1% aerogels. Our analysis indicates that, among the three models, the Langmuir isotherm model fits most accurately. Consequently, Figure S12a-j illustrates the nonlinear relationship between the equilibrium adsorption capacity (qe) and the equilibrium concentration (Ce), highlighting the applicability of the Langmuir isotherm model for describing monolayer adsorption processes on the surface of the adsorbents. This comprehensive analysis showcases the versatility of the isotherm models in predicting adsorption behaviors across a range of pollutants and adsorbents. Notably, Ach-1% aerogel exhibits superior adsorption capacity (q_{max}) for all studied adsorbates compared to ASB, with increases of 3.21, 3.42, 1.73, 1.56, and 1.13 times for MB, CV, Pb(II), U(VI), and As(III), respectively, as detailed in Table 1 (Tables S3 to S7).

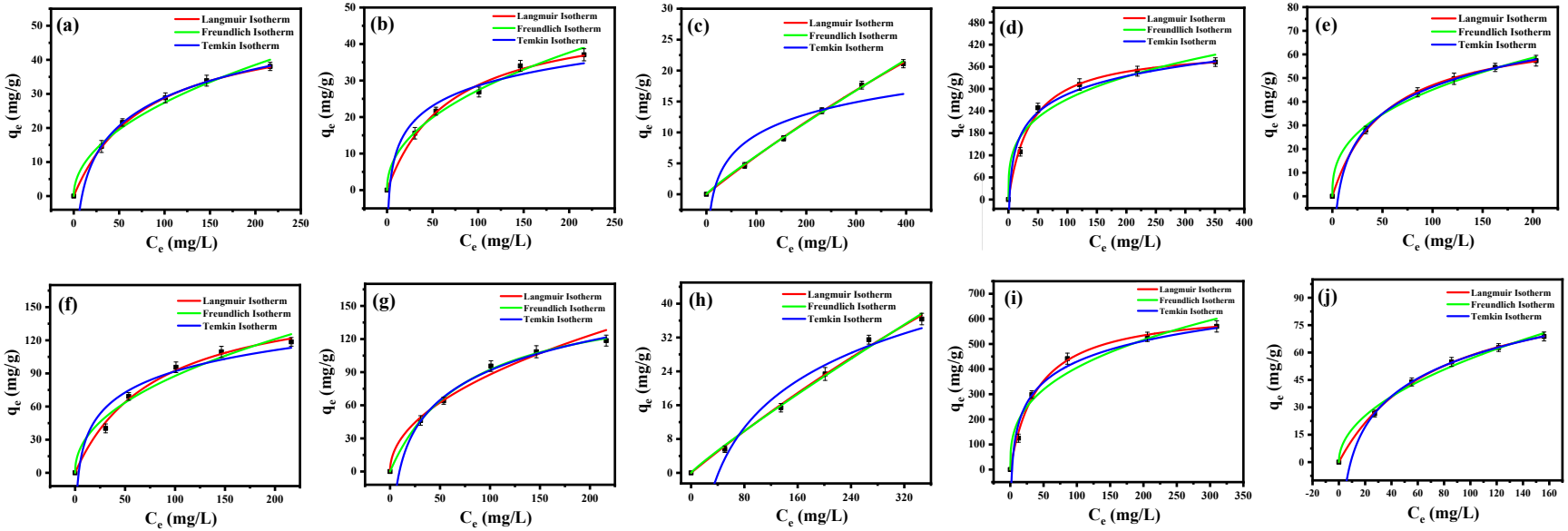

Figure S11: Langmuir, Freundlich, and Temkin adsorption isotherm models of adsorbed onto (a) MB on the ASB aerogel, (b) CV on the ASB aerogel, (c) Pb(II) on the ASB aerogel, (d) U(VI) on the ASB aerogel, (e) As(III) on the ASB aerogel, (f) MB on the Ach-1% aerogel, (g) CV on the Ach-1% aerogel, (h) Pb(II) on the Ach-1% aerogel, (i) U(VI) on the Ach-1% aerogel, and (j) As(III) on the Ach-1% aerogel.

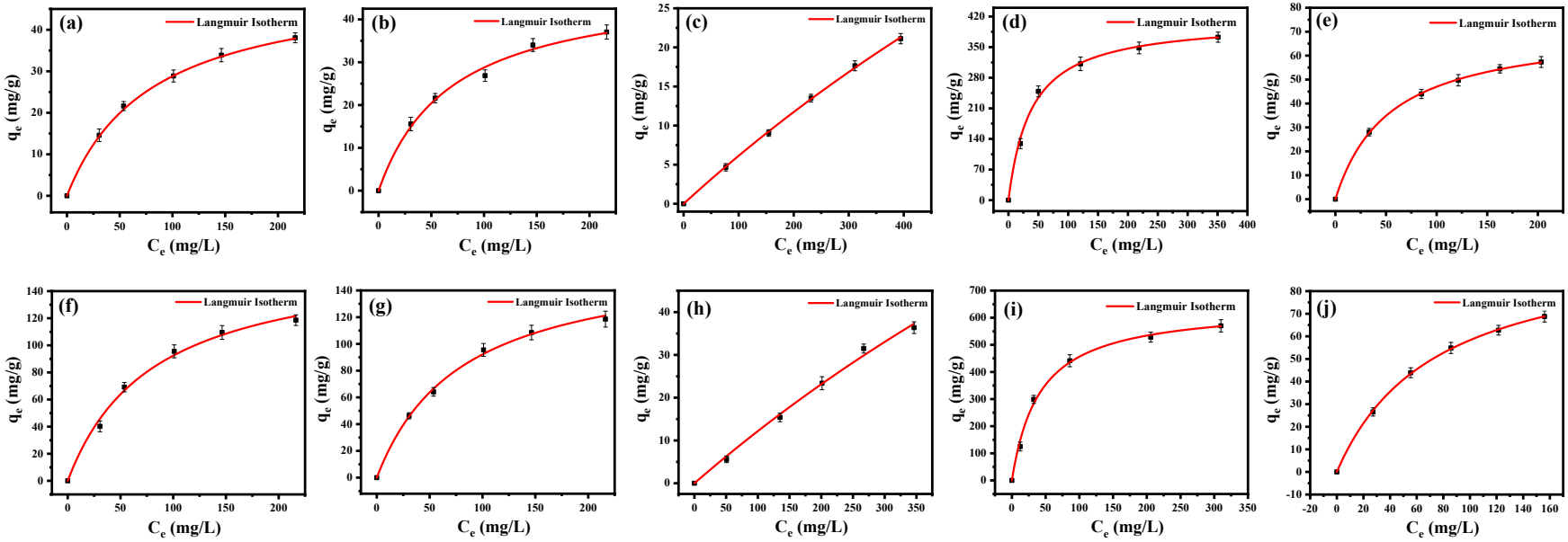

Figure S12: Langmuir isotherm model fitting of adsorbed onto (a) MB on the ASB aerogel, (b) CV on the ASB aerogel, (c) Pb(II) on the ASB aerogel, (d) U(VI) on the ASB aerogel, (e) As(III) on the ASB aerogel, (f) MB on the Ach-1% aerogel, (g) CV on the Ach-1% aerogel, (h) Pb(II) on the Ach-1% aerogel, (i) U(VI) on the Ach-1% aerogel, and (j) As(III) on the Ach-1% aerogel.

Table S3: Adsorption of MB by Adsorbents ASB and Ach-1% aerogel Obtained from the Langmuir, Freundlich, and Temkin Isotherm Models.

Adsorption Isotherms	Isotherm parameters	AN aerogel	AC aerogel	Nch-0.5%	Cch-0.5%	Ach-0.5%	Nch-1%	Cch-1%
Langmuir	R^2	0.9980	0.9928	0.9963	0.9983	0.9947	0.9947	0.9928
	Q_{max} (mg/g)	36.0952	39.0695	66.8056	55.1982	109.1159	100.2512	113.3009
	K_L (L/mg)	0.0135	0.0105	0.0124	0.0127	0.0124	0.0124	0.0105
	Chi-square	0.2461	0.9266	1.7663	0.8142	5.8907	4.9678	7.7928
Freundlich	R^2	0.9791	0.9846	0.9811	0.9506	9.9811	0.9812	0.9846
	K_F (mg/g)	2.2266	1.7278	3.6856	6.3549	6.0199	5.5247	5.0105
	1/n	0.4741	0.5222	0.4904	2.9958	0.4904	0.4906	0.5222
	n	2.1093	1.9148	2.0390	0.3338	2.0391	2.0384	1.9148
	Chi-square	0.9900	0.7886	2.9903	5.6572	7.9775	6.7255	6.6324
Temkin	R^2	0.9088	0.8905	0.9041	0.9471	0.9041	0.9041	0.8950
	Q_{max} (mg/g)	5.8663	6.0566	10.7066	9.2164	17.4875	16.0645	17.5642
	Kt (L/mg)	0.3412	0.2831	0.3189	0.3386	0.3189	0.3187	0.2831
	Chi-square	4.9466	6.1562	17.4005	6.8265	46.4203	39.1943	51.7733

Table S4: Adsorption of CV by Adsorbents ASB and Ach-1% aerogel Obtained from the Langmuir, Freundlich, and Temkin Isotherm Models.

Adsorption Isotherms	Isotherm parameters	AN aerogel	AC aerogel	Nch-0.5%	Cch-0.5%	Ach-0.5%	Nch-1%	Cch-1%
Langmuir	R^2	0.9980	0.9981	0.9970	0.9984	0.9947	0.9936	0.9957
	Q_{max} (mg/g)	26.2904	60.0788	48.7804	49.2827	109.1620	98.5253	75.6094
	K_L (L/mg)	0.0466	0.0177	0.0490	0.0482	0.0124	0.0128	0.0469
	Chi-square	0.2007	17.5446	1.0349	5.629	5.8902	5.8593	3.5163
Freundlich	R^2	0.9275	0.9267	0.9243	0.9254	0.9812	0.9804	0.9972
	K_F (mg/g)	5.9227	6.0815	11.4402	11.4048	6.0159	5.6688	22.4370
	1/n	0.2717	0.3364	0.2651	0.2673	0.4906	0.4844	0.2143
	n	3.6797	2.5723	3.7724	3.7411	2.0384	2.0645	4.6659
	Chi-square	1.6851	30.6696	5.9489	6.0222	7.9743	6.8183	2.3119
Temkin	R^2	0.9624	0.9528	0.9663	0.9658	0.9041	0.9058	0.9746
	Q_{max} (mg/g)	4.1539	14.6620	7.7003	7.8043	17.4923	15.8761	10.4512
	Kt (L/mg)	1.5817	0.1307	1.6634	1.6129	0.3187	0.3268	3.3778
	Chi-square	0.9736	19.7395	2.9199	3.0438	46.4699	37.5045	28.8508

Table S5: Adsorption of Pb(II) by Adsorbents ASB and Ach-1% aerogel Obtained from the Langmuir, Freundlich, and Temkin Isotherm Models.

Adsorption Isotherms	Isotherm parameters	AN aerogel	AC aerogel	Nch-0.5%	Cch-0.5%	Ach-0.5%	Nch-1%	Cch-1%
Langmuir	R^2	0.9964	0.9984	0.9935	0.9952	0.9943	0.9924	0.9955
	Q_{max} (mg/g)	39.0042	44.7836	59.8099	84.6839	159.8742	45.5299	75.6892
	K_L (L/mg)	0.0011	9.6108	9.5270	6.7708	5.6363	0.0019	8.4223
	Chi-square	0.0704	0.0329	0.2454	0.2181	0.5671	0.4160	0.2261
Freundlich	R^2	0.9927	0.9966	0.9896	0.9923	0.9924	0.9838	0.9925
	K_F (mg/g)	0.0951	0.0896	0.1128	0.0936	0.1262	0.276	0.1195
	1/n	0.8091	0.8252	0.8343	0.8802	0.9134	0.7164	0.8488
	n	1.2358	1.2118	1.1985	1.1360	1.0947	1.3957	1.1781
	Chi-square	0.1439	0.0716	0.3962	0.3498	0.7632	0.8948	0.3757
Temkin	R^2	0.813	0.8086	0.9855	0.7339	0.9640	0.8385	0.8023
	Q_{max} (mg/g)	3.0251	3.1440	7.6544	4.5849	11.2412	4.9568	4.8354
	Kt (L/mg)	0.0613	0.0598	0.0194	0.0555	0.0243	0.0718	0.0579
	Chi-square	2.0459	2.2731	0.5538	5.2992	3.6311	4.6022	5.5974

Table S6: Adsorption of U(VI) by Adsorbents ASB and Ach-1% aerogel Obtained from the Langmuir, Freundlich, and Temkin Isotherm Models.

Adsorption Isotherms	Isotherm parameters	AN aerogel	AC aerogel	Nch-0.5%	Cch-0.5%	Ach-0.5%	Nch-1%	Cch-1%
Langmuir	R^2	0.9996	0.9996	0.9986	0.99951	0.9996	0.9992	0.99704
	Q_{max} (mg/g)	343.1887	326.5701	452.7631	428.8377	434.2877	505.502	504.311
	K_L (L/mg)	0.0055	0.0062	0.0053	0.0058	0.0177	0.0054	0.00642
	Chi-square	2.9655	2.3610	1.794	6.1336	6.9123	1.314	5.60
Freundlich	R^2	0.9916	0.9862	0.9930	0.98929	0.9771	0.9921	0.9732
	K_F (mg/g)	8.5984	9.7745	10.9661	11.4834	40.3314	12.5911	15.3697
	1/n	0.5638	0.54097	0.5678	0.5557	0.3941	0.5645	0.5394
	n	1.7735	1.8485	1.7610	1.7994	2.5373	1.7713	1.8536
	Chi-square	69.0338	90.4926	91.4679	93.43118	49.14357	13.0686	50.7778
Temkin	R^2	0.8821	0.8887	0.8810	0.88452	0.9370	0.882	0.8891
	Q_{max} (mg/g)	55.0028	54.0187	71.942	69.7479	81.1509	80.8894	84.122
	Kt (L/mg)	0.1172	0.1263	0.1158	0.1203	0.2661	0.1170	0.1269
	Chi-square	395.0415	357.396	683.1672	621.1648	420.9181	855.962	862.984

9. U(VI) adsorption study in Seawater

Table S8 and Figure S13 provides a comprehensive analysis of the adsorption capacity and characteristics of U(VI) in seawater using two different adsorbents: ASB and Ach-1% aerogel. According to the Langmuir isotherm model, the R^2 values for both ASB (0.9997) and Ach-1% aerogel (0.9999) are very close to 1, indicating an excellent fit to this model, which suggests monolayer adsorption on a homogeneous surface. The maximum adsorption capacity (Qmax) is higher for Ach-1% aerogel (350.01 mg/g) compared to ASB (301.36 mg/g), demonstrating that Ach-1% aerogel has a greater capacity to adsorb U(VI) ions. Additionally, the Langmuir constant (K_L) is higher for the Ach-1% aerogel (0.0067 L/mg) than for the ASB (0.0039 L/mg), indicating a stronger affinity between the U(VI) ions and the Ach-1% aerogel. The experimental data and the Langmuir isotherm model agree well, with Ach-1% aerogel fitting slightly better. This is also indicated by the Chi-square values for ASB (1.6711) and Ach-1% aerogel (0.7908).

Comparatively, the Chi-square and R^2 values from the Freundlich and Temkin isotherm models suggest that the U(VI) adsorption in seawater follows the Langmuir isotherm model more closely than the other isotherms. This indicates that the adsorption process is likely monolayer and occurs on a homogeneous surface, making the Langmuir model the most appropriate for describing U(VI) adsorption by these adsorbents in seawater. Consequently, the exceptional performance of Ach-1% aerogel in terms of both adsorption capacity and affinity highlights its potential for practical applications in the extraction of U(VI) from seawater.

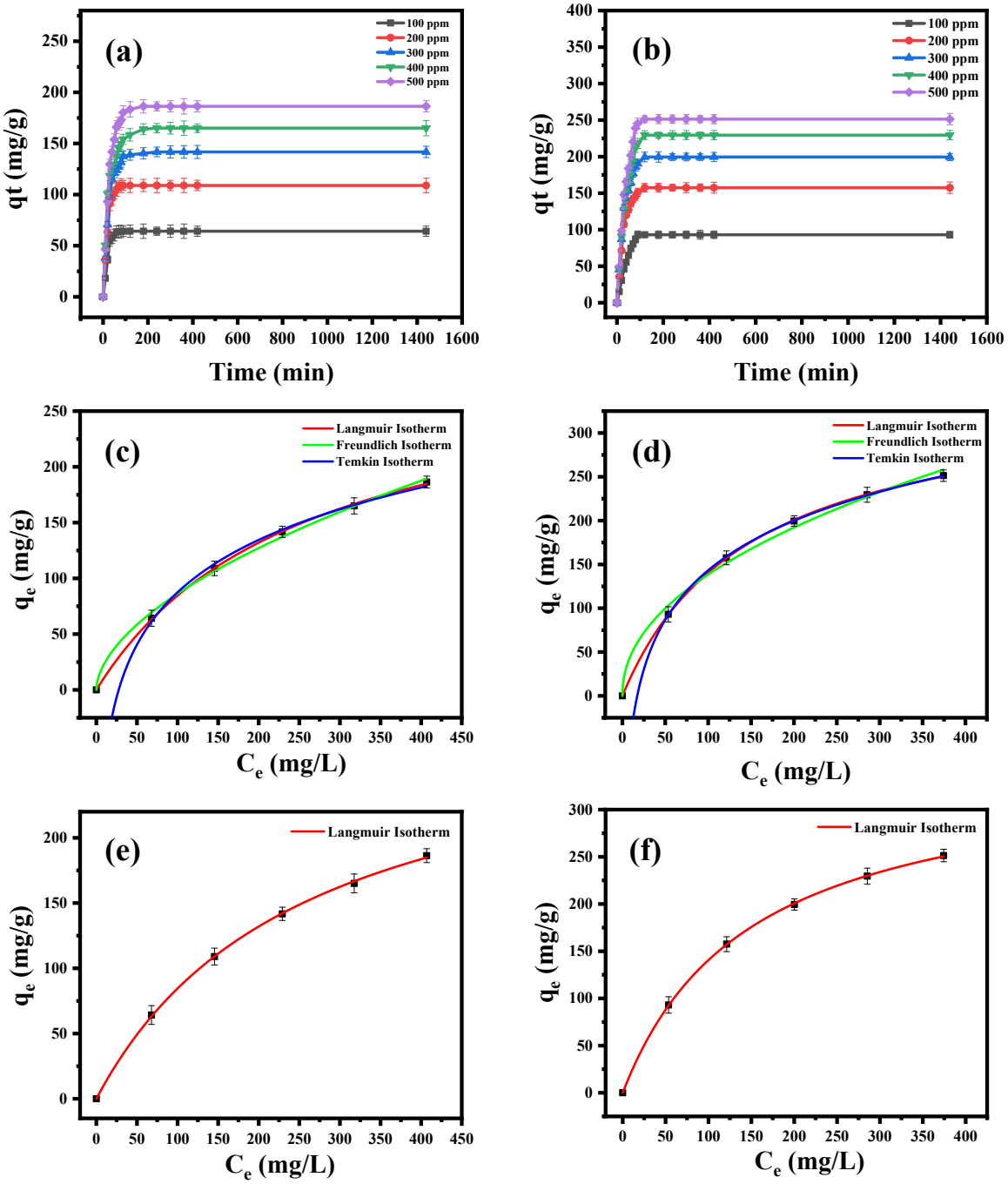

Figure S13: Plot of adsorption at time 't' (qt) versus incubation time of U(VI) in seawater for (a) ASB and (b) Ach-1% aerogel. Adsorption isotherm models (Langmuir, Freundlich, and Temkin) of U(VI) in seawater adsorbed onto (c) ASB and (d) Ach-1% aerogel. Langmuir adsorption isotherm models of U(VI) in seawater adsorbed onto (e) ASB and (f) Ach-1% aerogel.

Table S7: Adsorption of U(VI) in seawater by adsorbents ASB and Ach-1% aerogel, as described by the Langmuir, Freundlich, and Temkin isotherm models.

U(VI) seawater			
Adsorption Isotherms	**Isotherm parameters**	**ASB aerogel**	**Ach-1%**
Langmuir	R^2	0.9997	0.9999
	Q_{max} (mg/g)	301.36	350.01
	K_L (L/mg)	0.0039	0.0067
	Chi-square	1.6711	0.7908
Freundlich	R^2	0.9974	0.9946
	K_F (mg/g)	6.52	15.7659
	1/n	0.5607	0.4719
	n	1.7836	2.1191
	Chi-square	15.6358	59.9326
Temkin	R^2	0.9977	0.9898
	Q_m (mg/g)	67.8286	81.6289
	Kt (L/mg)	0.03632	0.05783
	Chi-square	10.7482	0.9592

10. Pseudo-second-order model

The adsorption of pollutants onto the ASB and Ach-1% aerogels followed pseudo-second-order kinetics, as described by Equation (6):

$$\frac{t}{q_t} = \frac{1}{k_2 q_e^{\,2}} + \frac{t}{q_e} \qquad \text{.....(6)}$$

The intercept of the linear plot is denoted as q_e whereas the slope of the linear plot gives the Pseudo-second-order rate constant (K_2), as shown in Figure 8a-e. q_e (mg/g) is the equilibrium adsorption potential at equilibrium and time t (min.).

11. Elovich kinetic model

Equation (7) expresses the non-linear form of the Elovich model.

$$q_t = \frac{1}{\beta}(\ln \alpha\beta t + 1) \qquad \text{.....(7)}$$

Where, q_t represents the amount adsorbed at time t, α is the initial adsorption rate, β is the desorption constant, and t is the time.

12. Intraparticle diffusion model. The linear form of the intraparticle diffusion model is given by Equation (8):

$$q_t = k_i t^{1/2} + C \qquad \text{.....(8)}$$

where *ki* is the intraparticle diffusion rate constant (g/mg. $\text{min}^{1/2}$), and *C* represents the intercept. Figure S14 represents the plot of qt against time of elovich model for ASB and Ach-1% aerogel.

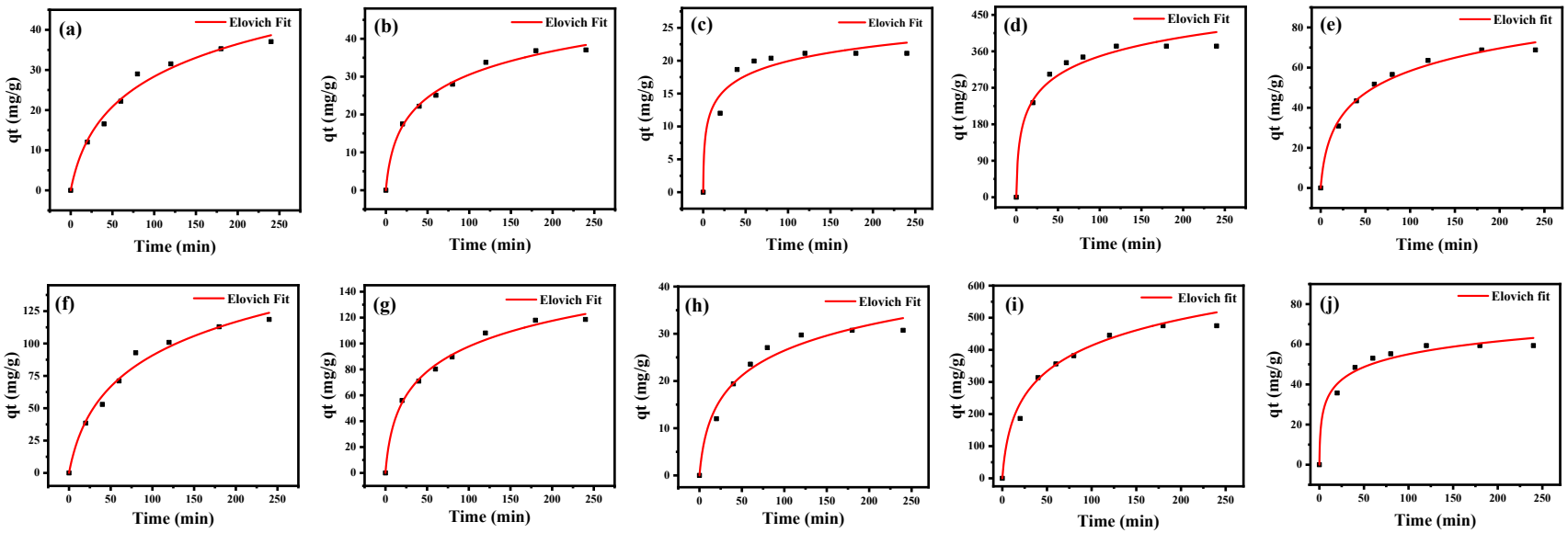

Figure S14: Elovich model parameters for the adsorption of dyes and heavy metals onto ASB and Ach-1% aerogel. The figure show adsorption data for (a) MB dye, (b) CV dye, (c) Pb(III), (d) U(VI), and (e) As(III).

13. Intraparticle diffusion model. When the commonly used Weber- Morris plot of qt vs $t^{1/2}$ reveals a straight line, only intra-particle diffusion is the influence for process of adsorption (Figure S15). If the plot reveals multiple processes at once data show multi-linear plots. The initial steeper area of the curve represents the preliminary stages of adsorption, where it is thought that the external mass transfer resistance encompassing the components is only important at that point. The second linear section controls intra-particle diffusion during the stage of progressive adsorption.

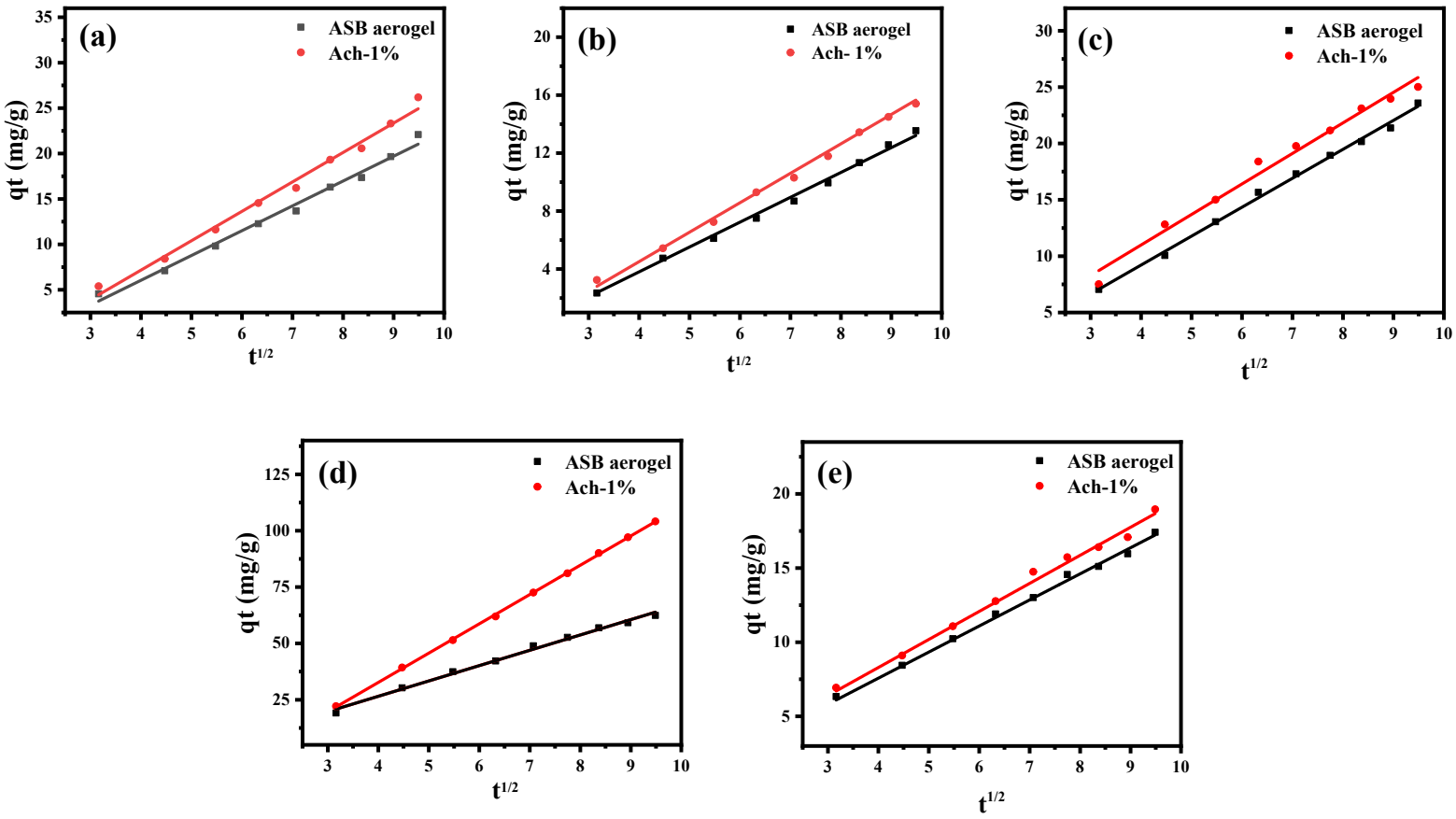

Figure S15: Intraparticle diffusion linear form model parameters for the adsorption of dyes and heavy metals onto ASB and Ach-1% aerogel. The figure show adsorption data for (a) MB dye, (b) CV dye, (c) Pb(III), (d) U(VI), and (e) As(III).

14. Regeneration of Saturated Adsorbents. Following third cycle, as shown in Figure S16, the ASB aerogel adsorption rate somewhat declines, and when the cycles are complete, the MB and CV dyes achieve 90 and 84%, accordingly, adsorption rates. Its outcomes also showed that adsorbents are able to be employed multiple times as an effective adsorption approach for the purification process of dye wastewater[78].

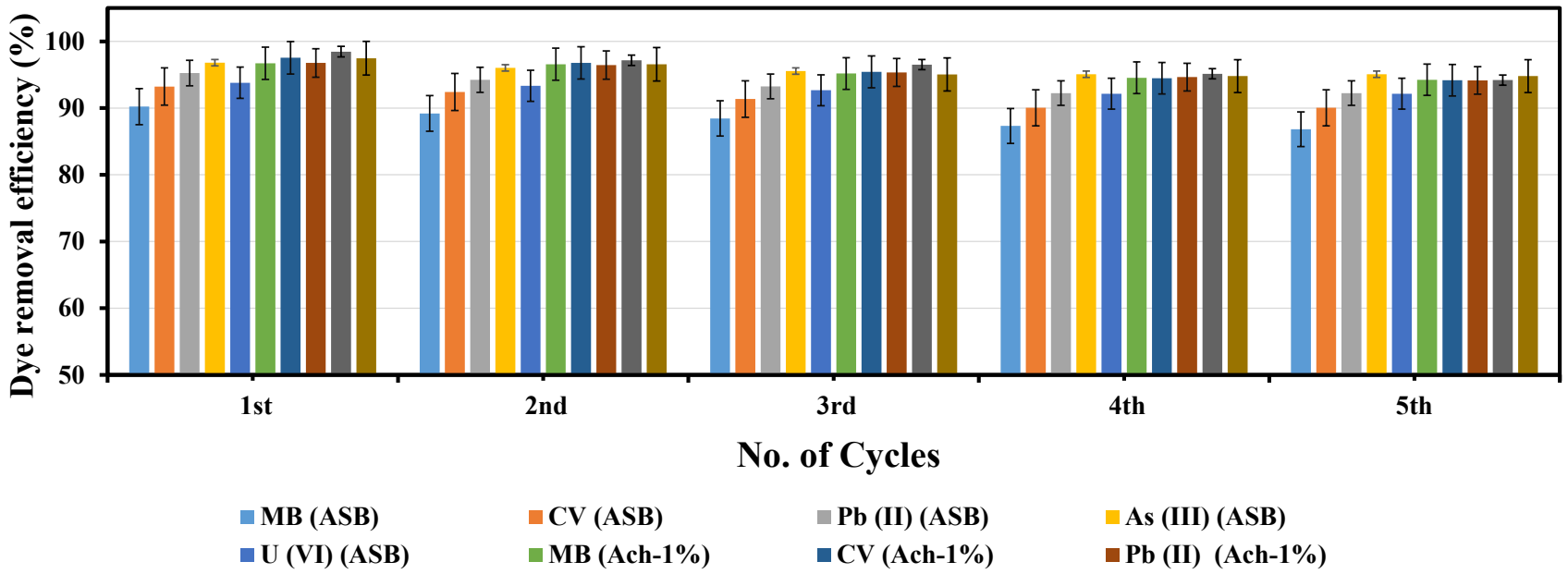

Figure S16: Removal efficiency and recyclability of ASB and Ach-1% Aerogel for heavy metal ions and dyes over four consecutive cycles. This study includes MB, CV, Pb(II), U(VI), and As(III).